

This is the accepted manuscript made available via CHORUS. The article has been published as:

Quantum phases of two-component bosons with spin-orbit coupling in optical lattices

Daisuke Yamamoto, I. B. Spielman, and C. A. R. Sá de Melo

Phys. Rev. A **96**, 061603 — Published 26 December 2017

DOI: [10.1103/PhysRevA.96.061603](https://doi.org/10.1103/PhysRevA.96.061603)

Quantum Phases of Two-Component Bosons with Spin-Orbit Coupling in Optical Lattices

Daisuke Yamamoto¹, I. B. Spielman², C. A. R. Sá de Melo^{2,3}

¹*Department of Physics and Mathematics, Aoyama-Gakuin University, Sagami-hara, Kanagawa 252-5258, Japan*

²*Joint Quantum Institute, National Institute of Standards and Technology,
and University of Maryland, Gaithersburg, Maryland 20899, USA and*

³*School of Physics, Georgia Institute of Technology, Atlanta, Georgia 30332, USA*

(Dated: November 25, 2017)

Ultracold bosons in optical lattices are one of the few systems where bosonic matter is known to exhibit strong correlations. Here we push the frontier of our understanding of interacting bosons in optical lattices by adding synthetic spin-orbit coupling, and show that new kinds of density- and chiral-orders develop. The competition between the optical lattice period and the spin-orbit coupling length – which can be made comparable in experiments – along with the spin hybridization induced by a transverse field (i.e., Rabi coupling) and interparticle interactions create a rich variety of quantum phases including uniform, non-uniform and phase-separated superfluids, as well as Mott insulators. The spontaneous symmetry breaking phenomena at the transitions between them are explained by a two-order-parameter Ginzburg-Landau model with multiparticle umklapp processes. Finally, in order to characterize each phase, we calculated their experimentally measurable crystal momentum distributions.

PACS numbers: 67.85.-d, 67.85.Hj, 67.85.Fg

The physics of spin-orbit coupling (SOC), which links the spin and momentum degrees of freedom in quantum particles, is ubiquitous in nature, ranging from the microscopic world of atoms, such as Hydrogen, to macroscopic solid materials, such as semiconductors. Recently, the effects of SOC have been explored in condensed matter physics in connection with topological insulators [1], as well as with topological superconductors [2], and superconductors without inversion symmetry [3]. In these naturally occurring systems, it is very difficult to control the magnitude of SOC and yet more difficult to study correlated bosons. However it is now possible to create controllable artificial SOC for trapped ultracold fermionic and bosonic atoms [4–9], the physics of which was recently analyzed theoretically in the continuum limit [4, 10–13] and one-dimensional (1D) optical lattices [14, 15]. In these cases weak coupling effects were considered, however one of the emerging frontiers in this broad area of physics is the interplay of the spin-orbit and lattice characteristic lengths, which can be made comparable in optical lattice systems, where additional contributions from a Zeeman field and strong local interaction-play an important role [16].

In this Rapid Communication, we obtain first the ground-state phase diagrams for two-component (\uparrow, \downarrow) bosons in the presence of artificial SOC, an effective Zeeman field (created from Rabi coupling and detuning), and local interactions. With zero detuning, we identify four phases: uniform, non-uniform and phase-separated superfluids, along with Mott insulating phases, depending on interactions. Secondly, we develop a Ginzburg-Landau theory for further characterizing these phases. Lastly, we calculate their crystal momentum distributions, which can be compared with experiments.

To describe the quantum phases of two-component

bosons with SOC, we begin by introducing the independent particle Hamiltonian

$$\hat{\mathcal{H}}_0 = \sum_{\mathbf{k}} \begin{pmatrix} \hat{b}_{\mathbf{k}\uparrow}^\dagger & \hat{b}_{\mathbf{k}\downarrow}^\dagger \end{pmatrix} \begin{pmatrix} \epsilon_{\mathbf{k}\uparrow} - \mu & \hbar\Omega/2 \\ \hbar\Omega/2 & \epsilon_{\mathbf{k}\downarrow} - \mu \end{pmatrix} \begin{pmatrix} \hat{b}_{\mathbf{k}\uparrow} \\ \hat{b}_{\mathbf{k}\downarrow} \end{pmatrix} \quad (1)$$

in momentum space. Here, $\epsilon_{\mathbf{k}s} = -2t[\cos(k_x + sk_T) + \cos k_y + \cos k_z] + s\hbar\delta/2$ for a three-dimensional (3D) optical lattice and $\mathbf{k}_T = (k_T, 0, 0)$ is the SOC momentum. The length scale $2\pi/k_T$ is of the order of the optical lattice spacing a , chosen to be one. The operator $\hat{b}_{\mathbf{k}s}^\dagger$ describes a creation of $s \in \{\uparrow, \downarrow\} \equiv \{+, -\}$ boson with momentum \mathbf{k} . The chemical potential μ tunes the average particle density $\rho = \rho_\uparrow + \rho_\downarrow \equiv \sum_{\mathbf{k}s} \langle \hat{b}_{\mathbf{k}s}^\dagger \hat{b}_{\mathbf{k}s} \rangle / M$ with M being the number of lattice sites. In cold-atom experiments, the effective Zeeman energy $\boldsymbol{\Omega} \cdot \hat{\mathbf{F}}$ with $\boldsymbol{\Omega} = (\Omega, 0, \delta)$ and $\hat{\mathbf{F}}$ being the total angular momentum operator for spin-1/2 has two parts: spin flips through the Rabi frequency Ω and a Zeeman shift via the detuning δ . The Hamiltonian above can be engineered in the laboratory either through Raman processes [4, 5, 17] or via radio-frequency chips [18, 19].

The diagonalization of $\hat{\mathcal{H}}_0$ gives two energy branches

$$E_{\mathbf{k}\pm} = \left(\epsilon_{\mathbf{k}\uparrow} + \epsilon_{\mathbf{k}\downarrow} - 2\mu \pm \sqrt{(\epsilon_{\mathbf{k}\uparrow} - \epsilon_{\mathbf{k}\downarrow})^2 + (\hbar\Omega)^2} \right) / 2.$$

For $\delta = 0$ and small $\hbar\Omega/t$, the lower branch $E_{\mathbf{k}-}$ has two degenerate minima at $k_x \approx \pm k_T$ and $k_y = k_z = 0$. The two minima approach as Ω is increased, and eventually they collapse into a single minimum at $\mathbf{k} = \mathbf{0}$ when $\hbar\Omega/t \geq 4 \sin k_T \tan k_T$. This double-minimum structure, the introduction of a new length scale $1/k_T$ and the interactions between particles

$$\hat{\mathcal{H}}_{\text{int}} = \frac{1}{2} \sum_{\mathbf{k}\mathbf{q}} \sum_{ss'} U_{ss'} \hat{b}_{\mathbf{k}s}^\dagger \hat{b}_{\mathbf{k}+\mathbf{q}s'}^\dagger \hat{b}_{\mathbf{k}-\mathbf{q}s'} \hat{b}_{\mathbf{k}s} \quad (2)$$

provide additional contributions that are absent in the standard spinless Bose-Hubbard system [20]. In this work, we explore the special case where the same spin repulsions U_{ss} are nearly identical ($U_{\uparrow\uparrow} \approx U_{\downarrow\downarrow} = U$), but the opposite spin repulsion is different from U , that is, $U \geq U_{\uparrow\downarrow} = U_{\downarrow\uparrow} \geq 0$. For instance, in the case of a mixture of the $m_F = 0$ (\downarrow) and $m_F = -1$ (\uparrow) states from the $F = 1$ manifold of ^{87}Rb , these repulsions are nearly identical ($U_{\uparrow\uparrow} \approx U_{\downarrow\downarrow} \approx U_{\uparrow\downarrow}$) [21].

We first investigate the regime of weak repulsive interactions ($U \ll t\rho$). The bosonic fields $\hat{b}_{\mathbf{k}s}$ can be written as $\hat{b}_{\mathbf{k}s} = \sum_q' \sqrt{M} \psi_{qs} \delta_{\mathbf{k}=(q,0,0)} + \hat{a}_{\mathbf{k}s}$, where $\sqrt{M} \psi_{qs}$ and $\hat{a}_{\mathbf{k}s}$ describe the Bose-Einstein condensate (BEC) with momentum $\mathbf{k} = (q, 0, 0)$ and the residual bosons outside the condensate, respectively. Considering the single and double minima features of $E_{\mathbf{k}-}$ within the first Brillouin zone, we allow for multiple BECs with different momenta and take the sum \sum_q' to be over the set of possible momenta $\{q\}$ along the $(k_x, 0, 0)$ direction. The energy per site of the condensates is

$$\frac{E_0}{M} = \sum_q' \begin{pmatrix} \psi_{q\uparrow}^* & \psi_{q\downarrow}^* \end{pmatrix} \begin{pmatrix} \epsilon_{\mathbf{k}\uparrow} - \mu & \hbar\Omega/2 \\ \hbar\Omega/2 & \epsilon_{\mathbf{k}\downarrow} - \mu \end{pmatrix} \begin{pmatrix} \psi_{q\uparrow} \\ \psi_{q\downarrow} \end{pmatrix} + \sum_{\{q_i\}}' \left[\frac{U}{2} \sum_s \psi_{q_1s}^* \psi_{q_2s}^* \psi_{q_3s} \psi_{q_4s} + U_{\uparrow\downarrow} \psi_{q_1\uparrow}^* \psi_{q_2\downarrow}^* \psi_{q_3\downarrow} \psi_{q_4\uparrow} \right], \quad (3)$$

where the sum $\sum_{\{q_i\}}'$ is over momenta q_i satisfying momentum conservation $q_1 + q_2 = q_3 + q_4 \pmod{2\pi}$.

After minimization of Eq. (3) with respect to ψ_{qs} and $\{q\}$, we find four different ground states as shown in Fig. 1(a) for the weak-coupling regime with parameters $U = t/\rho$, $U_{\uparrow\downarrow} = 0.9U$, and $k_T = 0.2\pi$. In the superfluid phases (SF_{\pm}), the set of BEC momenta $\{q\}$ consists of a single value ($\bar{q} > 0$ in SF_+ and $-\bar{q} < 0$ in SF_-) since the detuning δ tilts the single-particle spectrum and lifts the degeneracy of the double minima in $E_{\mathbf{k}-}$. In these “single- q ” states, the particle density is uniform, while the phase of the condensate spatially varies with pitch vector $(\pm\bar{q}, 0, 0)$. In the striped superfluid (ST) phase for relatively small $\hbar\Omega/t$, a BEC is formed with two different momenta $-\bar{q}_1$ and \bar{q}_2 due to a double-minimum dispersion in $E_{\mathbf{k}-}$. The interference of these two momenta leads to a non-uniform density profile along the x direction, resulting in a stripe pattern. Moreover, the scattering process under momentum conservation $q_1 + q_2 = q_3 + q_4$ with $q_3 = q_4 = -\bar{q}_1$ and $q_2 = \bar{q}_2$ (or vice-versa) gives rise to a higher harmonic component with $q_1 = -2\bar{q}_1 - \bar{q}_2$ (or $q_1 = \bar{q}_1 + 2\bar{q}_2$). Similar processes generate higher harmonics with interval $\bar{q}_1 + \bar{q}_2$, thus making the set $\{q\}$ have a large number of different momenta $-\bar{q}_1 + n(\bar{q}_1 + \bar{q}_2)$, where n is an integer. Higher harmonic generation is argued not to be qualitatively important in the continuum limit [13] or in weak 1D optical lattices [14], but in our case of deep 3D optical lattices this mechanism plays a crucial role in the stabilization of stripe phases commensurate with the underlying optical lattice, as discussed below.

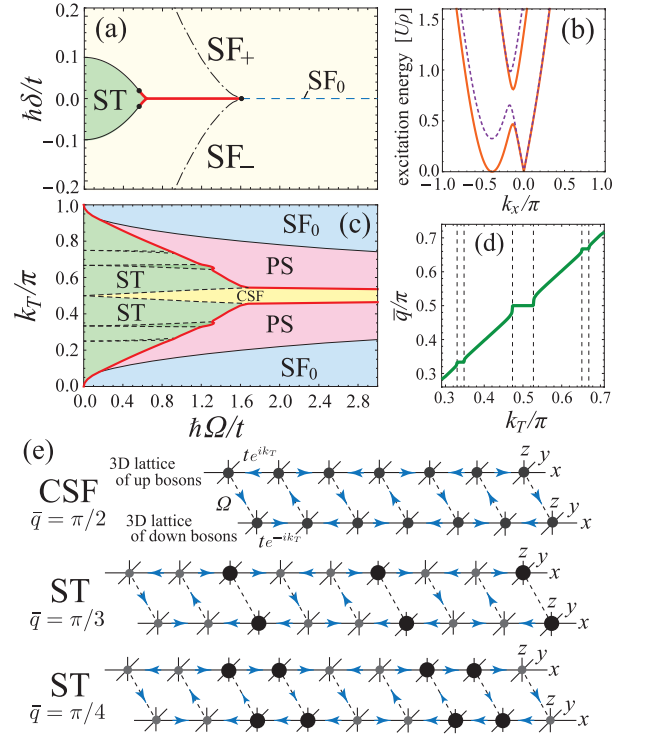


FIG. 1: (color online). Ground-state properties in the weak-coupling regime with $U/t = 1/\rho$ and $U_{\uparrow\downarrow} = 0.9U$. (a) Phase diagram of detuning δ versus Rabi frequency Ω for $k_T = 0.2\pi$. The thick red (thin black) curves denote first- (second-) order transitions and the black dots indicate multicritical points. In the $\delta > 0$ ($\delta < 0$) region to the left side of the dash-dotted line, the SF_- (SF_+) exists only as a metastable state. (b) Roton-like softening in the elementary excitations for quasi-momentum $\mathbf{k} = (k_x, 0, 0)$ and $\hbar\Omega/t = 0.4$. We set $\hbar\delta/t = 0.4$ (in SF_+) for the dotted lines and $\hbar\delta/t = 0.06$ (at the SF_+ -ST boundary) for the solid lines. (c) The k_T dependence of the ground state when $\rho_{\uparrow} = \rho_{\downarrow}$ ($\delta = 0$). The yellow and darker green regions limited by the black-dashed and red lines are the CSF and period-locked ST phases illustrated in (e). (d) The plateaux in \bar{q} of the CSF and period-locked ST phases as a function of k_T for $\hbar\Omega/t = 1.0$. The dashed lines denote the width of dominant plateaux with commensurate wavenumber \bar{q} . (e) Density (the size of dots) and chiral (the direction of arrows) patterns in the commensurate phases.

When $\hbar\Omega/t$ is large, the SF_+ and SF_- phases are continuously connected at $\delta = 0$ through the conventional superfluid (SF_0) with zero-momentum BEC. However, when $\hbar\Omega/t$ has intermediate values, a direct first-order transition from SF_+ to SF_- takes place, and thus the spin population difference $\rho_{\downarrow} - \rho_{\uparrow}$ exhibits a sudden jump from positive to negative. Therefore, in the experimental situation where $\rho_{\uparrow} = \rho_{\downarrow}$, the system is unstable against spatial phase separation (PS) of spin-down-rich SF_+ and spin-up-rich SF_- states.

The quadratic part of the Hamiltonian in terms of $\hat{a}_{\mathbf{k}s}$, $\hat{\mathcal{H}}_B = \sum_{\mathbf{k}} \hat{a}_{\mathbf{k}}^\dagger H_{\mathbf{k}}^{(2)} \hat{a}_{\mathbf{k}}$, is a generalized Bogoliubov Hamiltonian [22] and includes quantum fluctuations outside the condensate perturbatively. We diagonalize $\hat{\mathcal{H}}_B$ numeri-

cally [22, 23], and obtain the spectrum of elementary excitations. In Fig. 1(b) we show typical excitation spectra of the SF_+ states. In the SF_+ (SF_-) phase, the excitation energy of a roton-like minimum at a finite quasimomentum approaches zero as δ is decreased (increased), and the softening of the roton-like mode induces the ST transition, similar to the standard superfluid-supersolid transition [24]. The momentum of the roton-like excitations largely determines the characteristic reciprocal vector $\bar{q}_1 + \bar{q}_2$ of the ST state. Furthermore, the SF_{\pm} -ST transition can also be first order as indicated by the red solid line shown in Fig. 1(a). In this case, the energy gap of roton-like excitations jumps discontinuously to zero at the SF_{\pm}/ST boundary, playing the role of an order parameter for the first-order phase transition. The phase boundary where the roton minimum jumps discontinuously corresponds to the location of the Maxwell construction, where the free energy of the two phases have the same value. This is a generic feature of first order (discontinuous) phase transitions. The roton minimum has hysteretic behavior and remains finite in the region of metastability of the hysteresis curve before jumping to zero when sweeping from the SF_{\pm} to ST phases. Upon a reverse sweep from ST to SF_{\pm} the roton minimum remains at zero below the phase boundary and then jumps discontinuously back to a finite value at the end of the metastability region. Such behavior is similar to those encountered in continuum models of spin-orbit coupled Bose-Einstein condensates [25, 26].

The weak coupling phase diagram shown in Fig. 1(a) reveals ground states which are very similar to those in the continuum limit [4, 10–13], where the band structure due to the optical lattice is not important. However, the phase diagram of SOC momentum k_T/π versus $\hbar\Omega/t$ at $\rho_{\downarrow}=\rho_{\uparrow}$, shown in Fig. 1(c), illustrates the remarkable competition between the reciprocal vector of the underlying optical lattice and characteristic vector $\bar{q}_1 + \bar{q}_2$ of the ST phase. In the spin symmetric case ($\rho_{\uparrow} = \rho_{\downarrow}$), the two wavevectors \bar{q}_1 and \bar{q}_2 are equal, that is, $\bar{q}_1 = \bar{q}_2 \equiv \bar{q}$ leading to $\bar{q}_1 + \bar{q}_2 = 2\bar{q}$. The phase diagram in the range of $k_T = \pi$ to 2π is exactly the same as that of Fig. 1(c) since the lattice Hamiltonian $\hat{H}_0 + \hat{H}_{\text{int}}$ is invariant under the gauge transformation $\hat{b}_{\mathbf{k}s} \rightarrow \hat{b}_{\mathbf{k}+(\pi,0,0)s}$, as easily verified by direct substitution.

When k_T is nearly commensurate to the lattice reciprocal wavenumber 2π , such as $k_T \approx \pi/4$, $2\pi/3$, and $\pi/2$, the pitch vector \bar{q} of the ST state spontaneously takes an exact commensurate value over a finite range of k_T . Higher harmonic generation due to interactions and to umklapp process $q_1 + q_2 - q_3 - q_4 = 2\pi n$ with nonzero integer n favor commensurate phases, since their energy is lower than those of incommensurate ones. As a result, the curve of \bar{q}/π versus k_T/π exhibits multiple plateaux in the ST phase [Fig. 1(d)]. In particular, when $k_T \approx \pi/2$, BEC occurs with only two momenta $\pm\bar{q} = \pm\pi/2$ since all the higher-harmonics momenta are reduced to $\pm\pi/2$ due to the Brillouin zone periodicity. In this special case where $\bar{q}/\pi = 1/2$, the interference of the two momenta

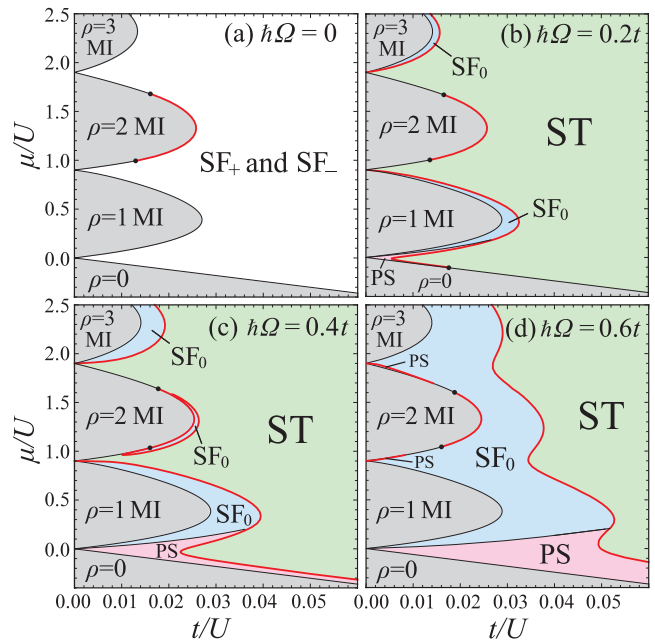


FIG. 2: (color online). Ground-state phase diagrams in the $(t/U, \mu/U)$ plane, obtained by the Gutzwiller self-consistent calculations for different values of $\hbar\Omega/t$. We set the other parameters as $U_{\uparrow\downarrow} = 0.9U$, $k_T = 0.2\pi$, and $\rho_{\uparrow} = \rho_{\downarrow}$ ($\delta = 0$).

does not lead to striped density pattern, but to Z_2 chiral symmetry breaking. This state is analogous to the chiral superfluid (CSF) state, which has been discussed in Bose-Hubbard ladders [27–30]. In the present case, the 3D lattices for the two spin components and the Rabi couplings play the role of rails and rungs, respectively, of a synthetic “two-leg ladder” in four (three spatial plus one extra spin) dimensions as illustrated in Fig. 1(e). For other commensurate ST phases, where \bar{q}/π takes an irreducible fraction ζ/η with ζ and η being integers, the superfluid phases break Z_η symmetry, but preserve a stripe pattern in the atom density. The stabilization of these commensurate phases is a specific feature of spin-orbit coupled systems in optical lattices with interactions and are completely absent in interacting continuum systems.

In addition to the interplay between different length/momentum scales discussed above, another particular feature of lattice systems is the existence of Mott insulator (MI) phases induced by strong interactions and commensurate particle fillings. To describe the Mott physics in the presence of SOC and Zeeman fields, we employ the Gutzwiller variational method [22]. Under the assumption that the ground state is given by a direct product state in real space, the Hamiltonian is mapped into inequivalent single-site problems connected via mean fields $\psi_{is} \equiv \langle \hat{b}_{is} \rangle$, where \hat{b}_{is} is the spin- s boson operator at lattice site i . To deal with the nonuniformity of the ST phases, we solve a set of self-consistency equations with 2000 mean fields ψ_{is} along the x direction for each spin and thus the momentum resolution is $\delta k_x \sim 0.001\pi$, while the y and z directions are assumed to be uniform [22]. In

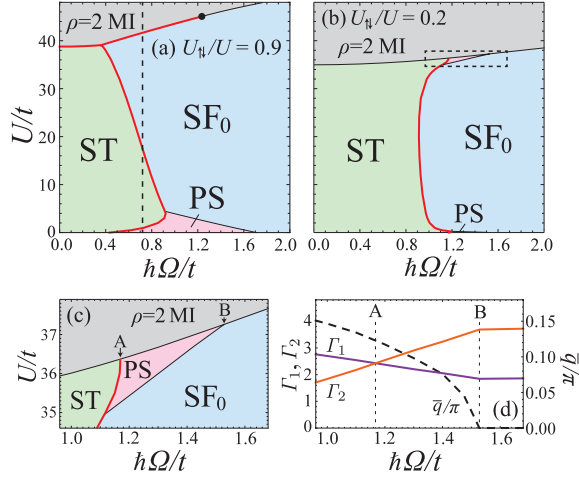


FIG. 3: (color online). Nonuniform superfluid-insulator transitions at $\rho = 2$ for (a) $U_{\uparrow\downarrow} = 0.9U$ and (b) $U_{\uparrow\downarrow} = 0.2U$. We set $k_T = 0.2\pi$ and $\rho_{\uparrow} = \rho_{\downarrow}$ ($\delta = 0$). The vertical dashed line in (a) marks $\hbar\Omega/t = 0.72$. The enlarged view of the region indicated by the dashed box in (b) is shown in (c). The fourth-order Ginzburg-Landau coefficients and the value of \bar{q} along the MI transition line of (c) are plotted in (d).

the ST phase, the inhomogeneous state is a result of the length scale introduced by the SOC, while in the absence of SOC a new length scale leading to a supersolid state appears due to long-range interactions [31].

Figure 2 shows phase diagrams in the μ/U - t/U plane for several values of Ω in the spin symmetric case $\rho_{\uparrow} = \rho_{\downarrow}$ ($\delta = 0$). In Fig. 2(a), where there is no spin hybridization ($\Omega = 0$), the phase boundaries of the MI lobes are identical to those in the absence of SOC [32] since the gauge transformation $\hat{b}_{\mathbf{k}s} \rightarrow \hat{b}_{\mathbf{k}+\mathbf{s}\mathbf{k}_T s}$ eliminates the momentum transfer \mathbf{k}_T from the problem. The even-filling Mott transitions become first order in a two-component Bose-Hubbard model for large inter-component repulsions (for example, $U_{\uparrow\downarrow} \gtrsim 0.68U$ when $\rho = 2$) [32–35]. In the superfluid phase outside the Mott lobes for $k_T \neq 0$, the spin-down and spin-up bosons independently form the SF_+ state with $\bar{q} = k_T$ and SF_- with $-\bar{q} = -k_T$, respectively.

When the Rabi frequency Ω is non-vanishing, the two spin components mix, forming a nonuniform ST state with two opposite momenta $-\bar{q}$ and \bar{q} and their associated higher harmonics. Figure 2(b) shows that the transition from the odd-filling MI to the ST phase occurs via an intermediate SF_0 state. A direct transition to the ST state occurs only for very small $\hbar\Omega/t$ (not shown: $\hbar\Omega/t \lesssim 0.04$ for $\rho = 1$). As seen in Figs. 2(c-d), when the value of $\hbar\Omega/t$ is increased, the SF_0 phase also emerges near the tip of the even-filling MI lobes, and eventually joins other SF_0 regions. The SF_+ and SF_- states only phase separate for small fillings $\rho \lesssim 1$ and a very narrow region around the $\rho = 2$ MI lobe for large $\hbar\Omega/t$.

To see the interplay between local correlations and spin mixing, we plot in Figs. 3(a-c) phase diagrams of U/t

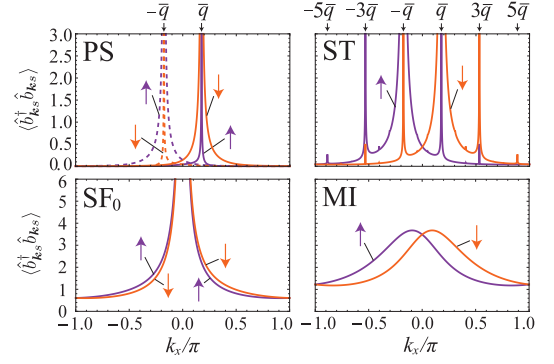


FIG. 4: (color online). The crystal momentum distributions $\langle \hat{b}_{\mathbf{k}s}^\dagger \hat{b}_{\mathbf{k}s} \rangle$ ($\mathbf{k} = (k_x, 0, 0)$) of the four different states along the line of $\hbar\Omega/t = 0.72$ in Fig. 3(a) (at $U/t = 0.5, 1.5, 30$, and 44). The contribution from SF_+ (SF_-) in the PS phase is plotted by the solid (dashed) lines.

versus $\hbar\Omega/t$ for fixed density $\rho = 2$. Moreover, the nature of the superfluid-insulator transition when $\rho_{\uparrow} = \rho_{\downarrow}$ can be described by the Ginzburg-Landau energy

$$\frac{E_{GL}}{M} = \xi(\mathbf{k}) (\Phi_I^2 + \Phi_{II}^2) + \frac{\Gamma_1}{2} (\Phi_I^4 + \Phi_{II}^4) + \Gamma_2 \Phi_I^2 \Phi_{II}^2 \quad (4)$$

up to fourth order of the order parameters $\Phi_I = |\Phi_{\bar{q}}|$ and $\Phi_{II} = |\Phi_{-\bar{q}}|$ for the BEC with $\mathbf{k} = (\pm\bar{q}, 0, 0)$. Note that the higher harmonics are negligible in the vicinity of the transition. The value of \bar{q} is determined so that the function $\xi(\mathbf{k})$ attains its minimum value $-\bar{\mu}$ at $\mathbf{k} = (\pm\bar{q}, 0, 0)$. When $\bar{\mu} > 0$, the bosons condense at \bar{q} and/or $-\bar{q}$ with $\bar{q} \neq 0$, or simply at $\bar{q} = 0$. For $\Gamma_1 < \Gamma_2$, the minimization of Eq. (4) gives $|\Phi_{\bar{q}}| \neq 0$ and $|\Phi_{-\bar{q}}| = 0$ (or vice-versa), and thus the Z_2 symmetry related to \bar{q} or $-\bar{q}$ is broken. In this case, the transition from MI to PS takes place. On the other hand, the condition $\Gamma_1 > \Gamma_2$ gives $|\Phi_{\bar{q}}| = |\Phi_{-\bar{q}}| \equiv \Phi \neq 0$, resulting in the transition to the ST or CSF phase. When \bar{q}/π is an irreducible fraction ζ/η , the relative phase $\phi = \text{Arg}(\Phi_{\bar{q}}/\Phi_{-\bar{q}})$ is determined by the minimization of additional η -particle umklapp process, $\Gamma'_\eta ((\Phi_{\bar{q}}^*)^\eta (\Phi_{-\bar{q}})^\eta + (\Phi_{-\bar{q}}^*)^\eta (\Phi_{\bar{q}})^\eta) \propto \cos \eta \phi$, which still has η -fold degeneracy. Thus the ST transition is associated with $U(1) \times Z_\eta$ symmetry breaking about the global and relative phases of $\Phi_{\pm\bar{q}}$.

The coefficients $\xi(q)$, Γ_1 , Γ_2 and Γ'_η are related to the microscopic system parameters in $\hat{\mathcal{H}}_0 + \hat{\mathcal{H}}_{\text{int}}$ by performing a perturbative expansion based on a direct-product MI state. For the specific relations see supplemental material [22]. We show in Fig. 3(d) the values of Γ_1 and Γ_2 along the line that separates the MI phase from the others as seen in Fig. 3(c). Note that if $\Gamma_1 < 0$ for $\Gamma_1 < \Gamma_2$ or $\Gamma_1 + \Gamma_2 < 0$ for $\Gamma_1 > \Gamma_2$, the condensates have a negative compressibility, and the transition becomes first-order.

To assist in the experimental identification of these quantum phases, Fig. 4 shows the crystal momentum distribution $\langle \hat{b}_{\mathbf{k}s}^\dagger \hat{b}_{\mathbf{k}s} \rangle$, which does not include the effects of Wannier functions, but can be easily extracted from standard momentum distribution measurements. We evalu-

ate $\langle \hat{b}_{\mathbf{k}s}^\dagger \hat{b}_{\mathbf{k}s} \rangle$ via the Bogoliubov Hamiltonian $\hat{\mathcal{H}}_B$ for the PS and ST states at relatively weak interactions, and via a generalized Holstein-Primakoff approach based on the Gutzwiller variational state for the SF_0 and MI states in the strongly coupled regime [22]. Since the PS state consists of independent domains of SF_+ and SF_- , we plot the simple average of the two contributions.

As seen in Figs. 4, the momentum distribution of the PS state exhibits two independent peaks around $\mathbf{k} = (\bar{q}, 0, 0)$ and $\mathbf{k} = (-\bar{q}, 0, 0)$, while the ST state shows additional peaks due to the higher harmonics. The SF_0 state exhibits a peak around $\mathbf{k} = \mathbf{0}$ as in the case of a standard uniform superfluid state, although the reflectional symmetry with respect to $k_x \rightarrow -k_x$ is absent for each spin component. In the MI state, only a broad peak is observed at the momenta where the condensation occurs in the neighboring superfluid state. The stark differences between these crystal momentum distributions also enable the direct imaging of the different phases present in inhomogeneous trapped systems.

In summary, we investigated the quantum phases of two-component bosons in optical lattices as a function of spin-orbit coupling, Rabi frequencies and interactions. In phase diagrams at zero detuning, we identified four different regions occupied by uniform, non-uniform and phase-separated superfluids or Mott insulators. Finally, we characterized these phases by calculating their crystal momentum distributions, which can be easily measured experimentally.

We thank N. E. Lundblad and D. Trypogeorgos for a careful reading of the manuscript. DY thanks the support of CREST, JST No. JPMJCR1673, and of KAKENHI from the Japan Society for the Promotion of Science: Grant No. 26800200. ISB thanks the support of AFOSRs Quantum Matter MURI, NIST, and the NSF through the PFC at the JQI. CARSDM acknowledges the support of JQI and NIST via its visitors program, the Galileo Galilei Institute for Theoretical Physics via a Simons Fellowship and the Aspen Center for Physics via NSF grant PHY1607611.

-
- [1] M. Z. Hasan and C. L. Kane, Rev. Mod. Phys. **82**, 3045 (2010).
 - [2] X.-L. Qi and S.-C. Zhang, Rev. Mod. Phys. **83**, 1057 (2011).
 - [3] *Non-Centrosymmetric Superconductors*, edited by E. Bauer and M. Sigrist (Springer-Verlag, Berlin, 2012).
 - [4] Y.-J. Lin, K. Jiménez-García, and I. B. Spielman, Nature **471**, 83 (2011).
 - [5] J.-Y. Zhang, S.-C. Ji, Z. Chen, L. Zhang, Z.-D. Du, B. Yan, G.-S. Pan, B. Zhao, Y.-J. Deng, H. Zhai, S. Chen, and J.-W. Pan, Phys. Rev. Lett. **109**, 115301 (2012).
 - [6] P. Wang, Z.-Q. Yu, Z. Fu, J. Miao, L. Huang, S. Chai, H. Zhai, and J. Zhang, Phys. Rev. Lett. **109**, 095301 (2012).
 - [7] L. W. Cheuk, A. T. Sommer, Z. Hadzibabic, T. Yefsah, W. S. Bakr, and M. W. Zwierlein, Phys. Rev. Lett. **109**, 095302 (2012).
 - [8] H. Zhai, Int. J. Mod. Phys. B, **26**, 1230001 (2012); V. Galitski and I. B. Spielman, Nature **494**, 49 (2013).
 - [9] J.-R. Li, Jeongwon Lee, W. Huang, S. Burchesky, B. Shteynas, F. Ç. Top, A. O. Jamison, and W. Ketterle, Nature **543**, 91 (2017).
 - [10] C. J. Wu, I. M. Shem, X. F. Zhou, Chin. Phys. Lett. **28**, 097102 (2011).
 - [11] T. L. Ho and S. Zhang, Phys. Rev. Lett. **107**, 150403 (2011).
 - [12] Y. Li, L. P. Pitaevskii, and S. Stringari, Phys. Rev. Lett. **108**, 225301 (2012).
 - [13] Y. Li, G. I. Martone, L. P. Pitaevskii, and S. Stringari, Phys. Rev. Lett. **110**, 235302 (2013).
 - [14] Z. Chen and Z. Liang, Phys. Rev. A **93**, 013601 (2016).
 - [15] G. I. Martone, T. Ozawa, C. Qu, and S. Stringari, Phys. Rev. A **94**, 043629 (2016).
 - [16] C. Hickey and A. Paramekanti, Phys. Rev. Lett. **113**, 265302 (2014).
 - [17] J. Higbie and D. M. Stamper-Kurn, Phys. Rev. Lett. **88**, 090401 (2002).
 - [18] N. Goldman, I. Satija, P. Nikolic, A. Bermudez, M. A. Martin-Delgado, M. Lewenstein, and I. B. Spielman, Phys. Rev. Lett. **105**, 255302 (2010).
 - [19] B. M. Anderson, I. B. Spielman, and G. Juzeliūnas, Phys. Rev. Lett. **111**, 125301 (2013).
 - [20] M. Greiner, O. Mandel, T. Esslinger, T. W. Hänsch, and I. Bloch, Nature (London) **415**, 39 (2002).
 - [21] A. Widera, F. Gerbier, S. Fölling, T. Gericke, O. Mandel, and I. Bloch, New J. Phys. **8**, 152 (2006).
 - [22] For technical details of calculations see Supplemental Material at [URL].
 - [23] J. H. P. Colpa, Physica **93A**, 327 (1978).
 - [24] S.-C. Ji, L. Zhang, X.-T. Xu, Z. Wu, Y. Deng, S. Chen, and J.-W. Pan, Phys. Rev. Lett. **114**, 105301 (2015).
 - [25] Giovanni I. Martone, Yun Li, Lev P. Pitaevskii and Sandro Stringari Physical Review A **86**, 063621 (2012).
 - [26] Renyuan Liao, Oleksandr Fialko, Joachim Brand, and Ulrich Zülicke, Physical Review A **92**, 043633 (2015).
 - [27] E. Orignac and T. Giamarchi, Phys. Rev. B **64**, 144515 (2001).
 - [28] A. Dhar, M. Maji, T. Mishra, R. V. Pai, S. Mukerjee, and A. Paramekanti, Phys. Rev. A **85**, 041602(R) (2012).
 - [29] M. Atala, M. Aidelsburger, M. Lohse, J. T. Barreiro, B. Paredes, and I. Bloch, Nat. Phys. **10**, 588 (2014).
 - [30] S. Greschner, M. Piraud, F. Heidrich-Meisner, I. P. McCulloch, U. Schollwöck, and T. Vekua, Phys. Rev. A **94**, 063628 (2016).
 - [31] V. W. Scarola, E. Demler, and S. Das Sarma, Physical Review A **73**, 051601(R) (2006).
 - [32] D. Yamamoto, T. Ozaki, C. A. R. Sá de Melo, and I. Danshita, Phys. Rev. A **88**, 033624 (2013).
 - [33] A. Kuklov, N. Prokof'ev, and B. Svistunov, Phys. Rev. Lett. **92**, 050402 (2004).
 - [34] P. Chen and M. F. Yang, Phys. Rev. B **82**, 180510(R) (2010).
 - [35] T. Ozaki, I. Danshita, and T. Nikuni, arXiv:1210.1370v1.